VO₂-hBN-graphene-based bi-functional metamaterial for mid-infrared bi-tunable asymmetric transmission and nearly perfect resonant absorption

HODJAT HAJIAN,[1,*] AMIR GHOBADI,[1,2] ANDRIY E. SEREBRYANNIKOV,[3,4] BAYRAM BUTUN,[1] GUY A. E. VANDENBOSCH,[4] AND EKMEL OZBAY[1,2,5,6]

[1]NANOTAM-Nanotechnology Research Center, Bilkent University, 06800 Ankara, Turkey
[2]Department of Electrical and Electronics Engineering, Bilkent University, 06800 Ankara, Turkey
[3]Faculty of Physics, Adam Mickiewicz University, 61-614 Poznan, Poland
[4]ESAT-TELEMIC, Katholieke Universiteit Leuven, B-3000 Leuven, Belgium
[5]Department of Physics and UNAM-Institute of Materials Science and Nanotechnology, Bilkent University, 06800 Ankara, Turkey
[6]e-mail: ozbay@bilkent.edu.tr
*Corresponding author: hodjat.hajian@bilkent.edu.tr

Bi-tunable asymmetric light transmission (AT) and nearly perfect resonant absorption functionalities are achieved by a Lorentz-reciprocal metamaterial for the operation at the mid-infrared (MIR) wavelengths and transverse magnetic polarization. The bi-tunable metamaterial with bi-functional features and a total thickness of 1.8 μm is based on an hBN/graphene/hBN heterostructure that is bounded by a Ge grating on the upper side and a hybrid VO₂/Au grating on the lower side. Through analytical calculations, we first investigate how the dispersion characteristics of the high-β hyperbolic phonon polaritons of hBN can be controlled and hybridized through the insulator (i-VO₂) to metal (m-VO₂) transition of VO₂ in a bare hBN/VO₂ heterostructure. Then, at the absence of graphene and owing to the support of the hybridized high-β modes, a broad and efficient AT with forward-to-backward contrast exceeding 40% is obtained by numerical calculations for the i-VO₂ case, as the first functionality of the structure. Moreover, it is found that for the m-VO₂ case, the device is no longer transmittive and a nearly perfect resonant absorption response, as the second functionality, is observed for backward illumination. Finally, by introducing multilayer graphene into the structure and considering the intermediate states of VO₂ in the calculations, the bi-tunable transmission and absorption characteristics of the device are investigated. We believe the designed metamaterial is well-suited for MIR optical diodes, sensors, and thermal emitters.   © 2019 Optical Society of America

https://doi.org/10.1364/JOSAB.36.001607

1. INTRODUCTION

Asymmetric light transmission (AT) [1–4] is known as the difference in transmission between forward and backward illumination (i.e., opposite directions) of a reciprocal electromagnetic device. It has been an active research topic due to its potential applications in integrated photonic systems for communications and information processing, such as directionally sensitive beam splitting [5], multiplexing [6], and optical interconnections [7]. Breaking the spatial inversion symmetry [1,2] and the time reversal symmetry [3,4] are two approaches that can be employed to achieve a strong forward-to-backward transmission contrast for an optical system. For the former case, the transmission of non-polarized and circularly/linearly polarized light through a device

is Lorentz-reciprocal and can be realized in diverse structures, such as waveguides [8], chiral/achiral metamaterials [1,9,10], metallic gratings with/without slits [5,6,11,12], metamaterials based on hyperbolic hole arrays [13], and graphene-based metamaterials [14–17]. Moreover, the combination of diffraction or subwavelength gratings with one- or two-dimensional photonic crystals [2,18,19] and hyperbolic metamaterials (HMMs) [20] can also lead to the observation of AT. For photonic crystal structures, the so-called dispersion–diffraction mechanism takes the lead, while the excitation of high-β modes with propagating/non-propagating features is responsible for the observation of AT while using HMMs.

Nearly perfect absorption is another distinguished aspect of photonic structures (including metamaterials) and plays a key

role in many applications, such as photodetectors, photovoltaics, sensing, and spectroscopy [21]. To realize nearly perfect absorption, reflectance is suppressed by matching the effective impedance of the metamaterial to that of the incident medium. Simultaneously, transmittance may be eliminated by introducing another metallic plate acting as a mirror [21,22]. Based on this mechanism, plasmonic/phononic absorbers operating in the visible to the lower frequency ranges with resonators of a different geometrical pattern have been designed and investigated comprehensively [23], including hexagonal boron nitride (hBN)- [24,25], graphene- [26,27], transition-metal dichalcogenide-based [28,29] absorbers and metasurfaces [30,31]. hBN is a natural hyperbolic material in the mid-infrared (MIR) region and is capable of supporting sub-diffractional volume-confined hyperbolic phonon polaritons (HP^2s) for transverse magnetic (TM) polarization [32–34].

Combining the HP^2s of hBN with surface plasmons polaritons of graphene (SP^2s) in graphene/hBN heterostructures leads to the support of hybrid plasmon–phonon polaritons, called SP^3 and HP^3 modes [35]. Because of the presence of graphene, dynamic tuning of the hyperbolic phonons of hBN is achievable by electrostatic gating in the resulted heterostructures. This feature makes the graphene/hBN systems a platform to achieve a new class of tunable waveguides [36,37] and light absorbers [38]. Vanadium dioxide (VO_2) can be another distinguished candidate for the dynamic tuning of HP^2 modes. As a phase change material, VO_2 exhibits a dramatic change in its complex refractive index due to a reversible insulator-to-metal transition (IMT) near room temperature. This material can be a promising building block in tunable or reconfigurable metamaterial light absorbers, switches, and modulators [39–42]. As a material with nonlinear optical response under high-power operation, VO_2 can also be realized in devices with AT characteristics [43,44]. Very recently, the hybridization between the HP^2 modes of hBN and the IMT of VO_2 (i.e., hybrid HP^2-IMT modes) has been experimentally investigated in hBN/VO_2 heterostructures [45,46]. It has been found that the HP^2s of hBN are insensitive to external stimuli and, therefore, by varying the temperature of the heterostructures, it is possible to dynamically tune the spectroscopic phonon resonances of hBN in both reststrahlen (RS) bands. The RS bands are categorized as RS-I and RS-II regions in which hBN with $\varepsilon_h = \text{diag}(\varepsilon_t, \varepsilon_t, \varepsilon_z)$ acts as a natural hyperbolic material with Type-I ($\varepsilon_z < 0$, $\varepsilon_t > 0$) and Type-II ($\varepsilon_z > 0$,

$\varepsilon_t < 0$) hyperbolicities [32]. Therefore, the gate tunable feature of SP^2 modes in graphene and the thermally tunable IMT characteristic of VO_2 provide us two degrees of freedom for the dynamic bi-tuning of the hybrid modes (called HP^3-IMT modes) in graphene/hBN/VO_2 heterostructures.

In this paper, we first analytically—by obtaining the TM dispersion relations and transmission characteristics of the hybrid modes using the transfer matrix method (TMM)—investigate how the phase transition of VO_2 affects the mode dispersion of the hyperbolic phonon polaritons of a bare hBN film; i.e., hybrid HP^2-IMT modes are examined. Using finite difference time domain (FDTD) calculations [47], we then design a metamaterial composed of a film of hBN that is covered on the upper side by a Ge grating and on the lower side by a hybrid grating composed of VO_2/Au that is placed on an Al_2O_3 substrate. The numerical calculations reveal that the device presents AT characteristics for the dielectric phase of VO_2 and exhibits a nearly perfect resonant absorption feature for backward illumination for the metal phase of VO_2; i.e., a bi-functional characteristic is observed. Next, considering multilayer graphene in the calculations, the dispersion properties of hybrid HP^3-IMT modes of a bare hybrid hBN/graphene/hBN/VO_2 (HGH/VO_2) heterostructure are investigated. Finally, in the presence of a multilayer graphene, the bi-tunable feature of the above-mentioned design (i.e., HGH/VO_2 bounded by the gratings) is investigated numerically for the different values of the chemical potential of graphene (μ) and intermediate states of IMT of VO_2 in the calculations. To the best of our knowledge, this is the first study on the analytical and numerical investigations HGH/VO_2-based systems with bi-tunable and bi-functional characteristics.

2. PHYSICAL MODEL

As mentioned above, the building block component of the final metamaterial device is a bi-tunable heterostructure composed of graphene, hBN, and VO_2; i.e., HGH/VO_2. A schematic of the HGH/VO_2 system is illustrated in Fig. 1(c). Figure 1(b) shows an hBN/VO_2 (HV) layered structure that provides us thermally switchable/tunable hybrid HP^2-IMT modes. A bare film of hBN with thickness t_h is also depicted in Fig. 1(a) as the elementary system. An Al_2O_3 substrate is considered for all these structures (shown in the schematics), and the upper cladding medium is air. The final metamaterial device is composed of an HGH heterostructure that is bounded by a Ge grating
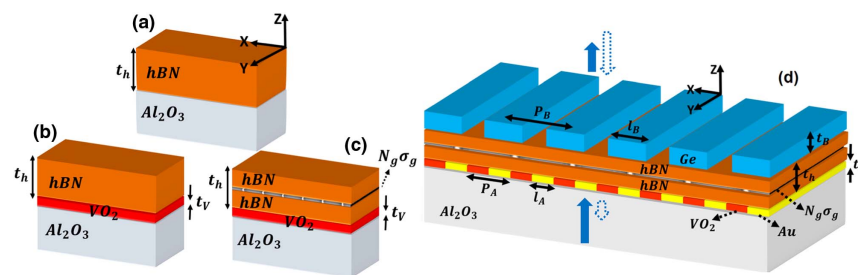
Fig. 1. (a) and (b) Schematics of a film of hBN with thickness t_h and a hBN/VO_2 heterostructure on an Al_2O_3 substrate, respectively. The thickness of the VO_2 film is t_V. (c) Schematic of an hBN/graphene/hBN/VO_2 multilayer system. (d) Drawing of the metamaterial device under our consideration. As shown in this panel, the building block component of the device is a HGH heterostructure that is bounded by a Ge grating on the upper side and a hybrid VO_2/Au grating on the lower side that is placed on an Al_2O_3 substrate.

with geometrical parameters of P_B, l_B, and t_B on the upper side, as well as a hybrid grating composed of alternating Au and VO_2 layers with periodicity P_A and Au width of l_A with thickness t_V on the lower side. The whole metamaterial device is placed on an Al_2O_3 substrate that makes our design more feasible for practical purposes [the schematic is shown in Fig. 1(d)].

The structures shown in Fig. 1(a) have been thoroughly investigated in the literature [36–38], thus we start with the derivation of HP²-IMT modes of the hBN/VO_2 structure. In our derivations, t_h and t_V denote the thickness of the hBN and VO_2 layers, respectively, and ε_V is the permittivity of VO_2 that is taken from experimental data reported by Ref. [39]. Considering the y component of the magnetic field as

$H_y(z)$

$$= \begin{cases} A e^{-q_A(z-t_h/2)}, & z > t_h/2 \\ h_1 e^{-q_h z} + h_2 e^{q_h z}, & -t_h/2 \leq z \leq t_h/2 \\ V_1 e^{q_V(z+t_h/2)} + V_2 e^{-q_V(z+t_h/2)}, & -t_V - t_h/2 \leq z \leq -t_h/2 \\ S e^{q_S(z+t_h/2)}, & z < -t_V - t_h/2 \end{cases}$$
(1)

and applying the boundary conditions for TM polarization [37], we arrive at the following dispersion relation of the hybrid HP²-IMT modes of the HV structure that is bounded by materials with ε_A and ε_S:

$$\tan h(q_V t_V) = \frac{-\Gamma_h + m_2 \Gamma_S}{\Gamma_h \Gamma_S - m_2}.$$
(2)

Here, $\Gamma_h = \frac{q_V \varepsilon_t}{\varepsilon_V q_h}$ $\Gamma_S = \frac{q_V \varepsilon_S}{\varepsilon_V q_S}$, $m_2 = \frac{m_1 - e^{q_h t_h}}{m_1 + e^{q_h t_h}}$, $m_1 = \frac{e^{-q_h t_h}(\frac{\varepsilon_A q_h}{q_A \varepsilon_t}-1)}{\frac{\varepsilon_A q_h}{q_A \varepsilon_t}+1}$, $q_h = \sqrt{\varepsilon_t(\beta^2 - \varepsilon_z \beta_0^2)/\varepsilon_z}$, $q_i = \sqrt{\beta^2 - \varepsilon_i \beta_0^2}(i = A, V, S)$, $\beta = k_x$, and $\beta_0 = \frac{\omega}{c}$, and $\varepsilon_h = \text{diag}(\varepsilon_t, \varepsilon_t, \varepsilon_z)$ is given by [32]

$$\varepsilon_m = \varepsilon_{\infty,m} \times \left[1 + \frac{\omega_{LO,m}^2 - \omega_{TO,m}^2}{\omega_{TO,m}^2 - \omega^2 - i\omega\Gamma_m}\right], \quad m = t, z, \quad (3)$$

where $\varepsilon_{\infty,x} = 2.95$, $\varepsilon_{\infty,z} = 4.87$, $\omega_{LO,x} = 1610$ cm⁻¹ ($\equiv 6.2$ µm), $\omega_{TO,x} = 1370$ cm⁻¹ ($\equiv 7.3$ µm), $\omega_{LO,z} = 830$ cm⁻¹, $\omega_{TO,z} = 780$ cm⁻¹, $\Gamma_x = 4$ cm⁻¹, and $\Gamma_z = 5$ cm⁻¹. It is noteworthy that for the case of removing the VO_2 film in the above calculations, Eq. (2) reduces back to the well-known dispersion relation of HP₂ modes supported by a film of hBN of thickness t_h [36] that is schematically shown in Fig. 1(a).

To be able to obtain the dispersion relation of the HGH/VO_2 structure [shown schematically in Fig. 1(c)], the presence of the graphene multilayer should be accounted for in the calculations. Taking H_y similarly to the one used in Eq. (1) and applying TM boundary conditions, we arrive at the following dispersion relation of the bi-tunable HP³-IMT modes supported by an HGH/VO_2 heterostructure:

$$\tan h(q_V t_V) = \frac{-\Gamma_h + m_5 \Gamma_S}{\Gamma_h \Gamma_S - m_5},$$
(4)

where $m_5 = \frac{m_4 - e^{q_h t_h}}{m_4 + e^{q_h t_h}}$, $m_4 = \frac{\frac{\alpha_g q_h}{\varepsilon_x} + m_3 + 1}{\frac{\alpha_g q_h}{\varepsilon_x} + m_3 - 1}$, $m_3 = \frac{m_1 + 1}{m_1 - 1}$, and $\alpha_g = \frac{N_g \sigma_g}{i\omega\epsilon_0}$, and N_g denotes the number of graphene layers in the multilayer graphene shown in Figs. 1(c) and 1(d) ($N_g = 1$

represents a single layer graphene). The optical conductivity of the graphene ($\sigma_g = \sigma_g^{intra} + \sigma_g^{inter}$), which is a function of frequency and temperature, can also be shown as [48]

$$\sigma_g^{intra}(\omega, T) = \frac{e^2}{4\hbar} \frac{i}{2\pi} \left\{ \frac{16 k_B T}{\hbar\Omega} \ln\left(2 \cosh\left(\frac{\mu}{2 k_B T}\right)\right) \right\},$$
(5a)

$$\sigma_g^{inter}(\omega, T) = \frac{e^2}{4\hbar} \left\{ \frac{1}{2} + \frac{1}{\pi} \arctan\left(\frac{\hbar\Omega - 2\mu}{2 k_B T}\right) - \frac{i}{2\pi} \ln \frac{(\hbar\Omega + 2\mu)^2}{(\hbar\Omega - 2\mu)^2 + (2 k_B T)^2} \right\},$$
(5b)

with $\Omega = \omega + i\tau^{-1}$; e is the electron charge, k_B is the Boltzmann constant, τ is electron relaxation time, and $\hbar$ is the Plank constant over 2π. In the case of removing graphene from the calculations (i.e., $\alpha_g \to 0$), Eq. (4) reduces back to Eq. (2). Moreover, the relaxation time of graphene is taken to be $\tau = 1$ ps in our calculations in this paper.

TMM is another analytical approach that we use to investigate mode hybridization and understand how the high-β hybrid HP³-IMT modes (HP²-IMT modes) can be strongly/weakly transmitted through the bare HGH/VO_2 system (hBN/VO_2 structure). By taking the appropriate form of H_y in each medium and applying the TM boundary condition at each interface, we arrive at $\Im = |t|^2$ as an analytical relation for electromagnetic light transmission through the considered heterostructures, with $t = 1/M_{11}$ and $M = \begin{bmatrix} M_{11} \\ M_{12} \end{bmatrix} = M_A^{-1}(M_{h1} M_{h2}^{-1})(M_{h3} M_{h4}^{-1})(M_{V1} M_{V2}^{-1}) M_S$. Here,

$$M_A = \begin{bmatrix} -ik_A/\varepsilon_A & ik_A/\varepsilon_A \\ 1 & 1 \end{bmatrix}, \qquad M_S = \begin{bmatrix} -ik_A/\varepsilon_A \\ 1 \end{bmatrix},$$
(6a)

$$M_{h1} = \begin{bmatrix} -ik_h/\varepsilon_x & ik_h/\varepsilon_x \\ 1 & 1 \end{bmatrix},$$

$$M_{h2} = \begin{bmatrix} -e^{ik_h t_h/2} & e^{-ik_h t_h/2} \\ e^{ik_h t_h/2} & e^{-ik_h t_h/2} \end{bmatrix},$$
(6b)

$$M_{h3} = \begin{bmatrix} -1 & 1 \\ 1 + \alpha_g & 1 - \alpha_g \end{bmatrix},$$

$$M_{h4} = \begin{bmatrix} -ik_h e^{ik_h t_h/2}/\varepsilon_x & ik_h e^{-ik_h t_h/2}/\varepsilon_x \\ e^{ik_h t_h/2} & e^{-ik_h t_h/2} \end{bmatrix},$$
(6c)

$$M_{V1} = \begin{bmatrix} -ik_V/\varepsilon_V & ik_V/\varepsilon_V \\ 1 & 1 \end{bmatrix},$$

$$M_{V2} = \begin{bmatrix} -ik_V e^{ik_V t_V}/\varepsilon_V & ik_V e^{-ik_V t_V}/\varepsilon_V \\ e^{ik_V t_V} & e^{-ik_V t_V} \end{bmatrix}.$$
(6d)

3. RESULTS

Investigation of the dispersion characteristics and the hybridization of HP² modes of hBN with IMT of VO_2 gives us a fair insight into the thermal switching of the hyperbolic phonon

polaritons of hBN by phase transition of VO_2. Note that here we choose $t_h = 600$ nm, $t_V = 200$ nm, and $\varepsilon_{A=\text{Air}} = 1$, and $\varepsilon_{S=Al_2O_3}$ is taken from Ref. [49]. Moreover, the results are presented within the RS-II band of hBN, i.e., 6.2–7.3 μm. Here we refer to the results related to the metal and insulator phases of VO_2 as m-VO_2 and i-VO_2, respectively. It is noteworthy that, following Ref. [39], the corresponding temperatures of the i-VO_2 and m-VO_2 phases are assumed to be 300 K and 358 K, respectively, and the results are presented for normal incidence of light. For the FDTD calculations [47], the material data are used for Ge and Au, and graphene is defined as a 2D sheet with the optical conductivity provided by Eq. (5). Moreover, VO_2 and hBN permittivities are introduced to the software as data files. Furthermore, an unit cell with periodic boundary condition in the X direction and a perfectly matched layer along the Z axis are employed, and the structure is excited by a broadband plane wave.

The dispersion characteristics of HP^2 modes supported by a film of hBN [the structure schematically shown in Fig. 1(a)] have been investigated in detail in recently published papers (see, e.g., Ref. [36]). However, in Figs. 2(a) and 2(b), we illustrate them in black curves for ease of comparison with the hybrid modes. For the structure depicted in Fig. 1(b), the hybrid HP^2-IMT modes are presented in blue [Fig. 2(a)] and red [Fig. 2(b)] lines for the i-VO_2 and m-VO_2 cases, respectively. As seen from the dispersion curves, the effect of the presence of VO_2 leads to the redshifting of the original HP^2 modes while not distorting the hyperbolic nature of the modes. This is in agreement with the recently reported results [45,46]. To get
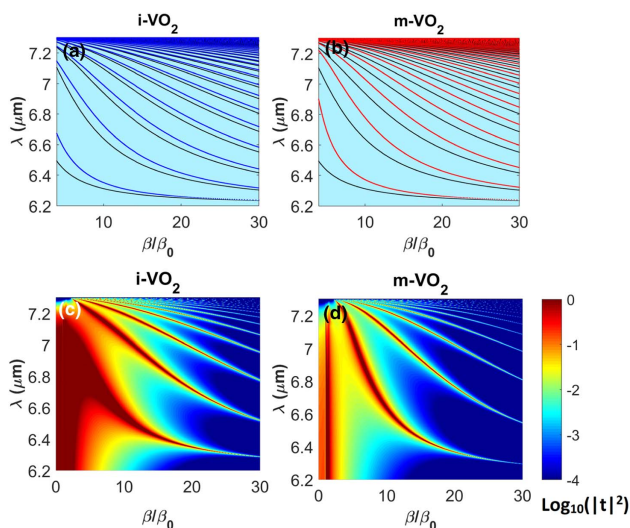

Fig. 2. (a) and (b) TM dispersion of hybrid HP^2-IMT modes supported by the hBN/VO_2 heterostructure shown in Fig. 1(b) with $t_h = 600$ nm and $t_V = 200$ nm for the i-VO_2 [solid blue lines in (a)] and m-VO_2 [solid red lines in (b)] cases. For ease of comparison, the dispersion of HP^2 modes of the bare hBN ($t_h = 600$ nm) of the structure shown in Fig. 1(a) is shown as black lines in these panels. (c) and (d) TMM-calculated TM-polarized light transmission, in a logarithmic scale, as a function of wavelength and normalized wavenumber for the structure shown in Fig. 1(b) for the i-VO_2 and m-VO_2 phases. The results are illustrated in the RS-II band of hBN.

more insight into the propagation of the hybrid modes inside the HV heterostructure [shown in Fig. 1(b)], TMM-calculated TM-polarized light transmissions for metal and insulator phases of VO_2 are illustrated in Figs. 2(c) and 2(d), respectively. Since the thickness of the considered film of hBN in the calculation is taken as 600 nm, the unpatterned hBN film is fairly transmittive inside the RS-II band for normal incidence. Therefore, for the i-VO_2 case, the HV structure can perfectly transmit light for normal incidence [see Fig. 2(c)], while, as observed from Fig. 2(d), due to the reflective/absorptive nature of VO_2 in the metallic phase, transmission of the HV structure is quite low for normal incidence. In perfect agreement with the dispersion curves of the hybrid HP^2-IMT modes shown in Figs. 2(a) and 2(b), Figs. 2(c) and 2(d) also highlight the point that the HV heterostructure is capable of supporting high-β propagating hybrid modes with transmittive characteristics in the Z direction.

After getting insight into the propagation characteristics of the hybrid modes supported by the bare HV system, now we investigate AT and the nearly perfect resonant absorption features of the metamaterial shown in Fig. 1(d) in the absence of graphene. At this stage, we focus only on the switching characteristic of VO_2 from insulator to metal phases. It should be noted that here, T_F and T_B denote transmission through the device at normal illuminations in the $+Z$ and $-Z$ directions, respectively. By taking the grating parameters shown in Fig. 1(d) as $P_B = 4$ μm, $l_B = 3$ μm, $P_A = 3$ μm, and $l_A = 1.5$ μm in the calculations (leading to the fundamental reciprocal lattice wavevectors of magnitude $G_A = 2\pi/P_A$ and $G_B = 2\pi/P_B$), we investigate the AT of the grating-bounded metamaterial in the absence of graphene in the second RS band of hBN. By these choices and employing the grating law $(2\pi/\lambda \sin(\theta) = \beta + nG_{A,B})$, G_A and G_B can couple normally incident light ($\theta = 0$) to a high-β hybrid HP^2-IMT mode that can be propagating/evanescent inside hBN (as a natural hyperbolic material) with a transverse wavevector located inside the β ranges corresponding to high/low transmission in Fig. 2(c). Here, θ is the angle of incident light with respect to the $+Z/-Z$ direction for forward/backward illumination, and $n = \pm 1, \pm 2, \ldots$. Similar to the mechanisms leading to AT for the metallic hyperbolic metamaterials [20], there are two conditions responsible for achieving asymmetric transmission. First, to enable the coupling of the wave incident on the metamaterial from side A (B) to an outgoing wave on side B (A) (having tangential wavevector β_{out}), G_A and G_B must satisfy the condition $|G_A - G_B/n| = \beta_{\text{out}} < \beta_0$. Second, to reach a lower transmission in the backward direction than in the backward one at a desired wavelength, G_B and $2G_B$ must be placed inside low-transmission regions ($|t|^2 < 0.05$) in Fig. 2(c). The resulting forward and backward transmissions through the i-VO_2 grating-bounded hBN for normal incidence are shown in Fig. 3(a) by the solid and dashed blue lines, respectively.

As shown in Fig. 3(a), there is a noticeable difference between light transmission for forward and backward illuminations for the i-VO_2 case in the RS-II band of hBN for which $T_{F,\text{max}}$ is observed at $\lambda = 6.6$ μm. At this wavelength, the corresponding values of G_A and G_B are $2.2\beta_0$ and $3 \times 1.34\beta_0$, respectively, which leads to $\beta_{\text{out}} = 0.86\beta_0$ and fully follows the
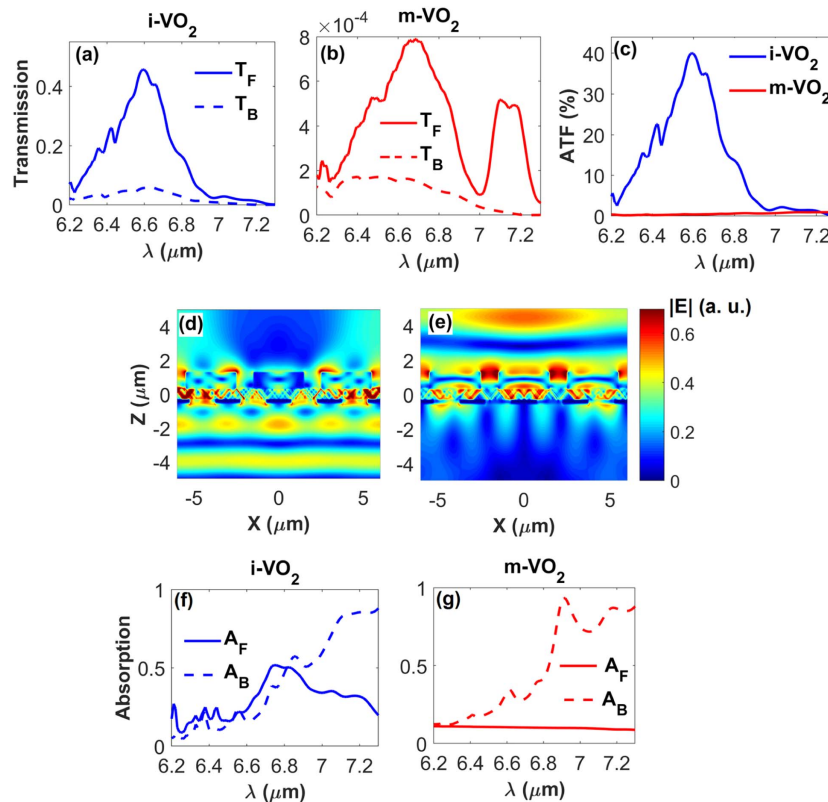
Fig. 3. Transmission and absorption characteristics of the device shown in Fig. 1(d) (in the absence of graphene) for $P_B = 4$ µm, $l_B = 3$ µm, $P_A = 3$ µm, and $l_A = 1.5$ µm for two insulating and metal phases of VO_2 and normal incidence. (a) and (b) Forward (solid line) and backward (dashed line) transmission of the grating bounded metamaterial for the i-VO_2 and m-VO_2 phases. (c) ATF of the device for both the i-VO_2 (solid blue line) and m-VO_2 (solid red line) cases. Near-field mode profiles for (d) forward and (e) backward illuminations at $\lambda = 6.9$ µm. Forward (solid line) and backward (dashed line) absorption of the device for the (f) i-VO_2 and (g) m-VO_2 cases are also shown.
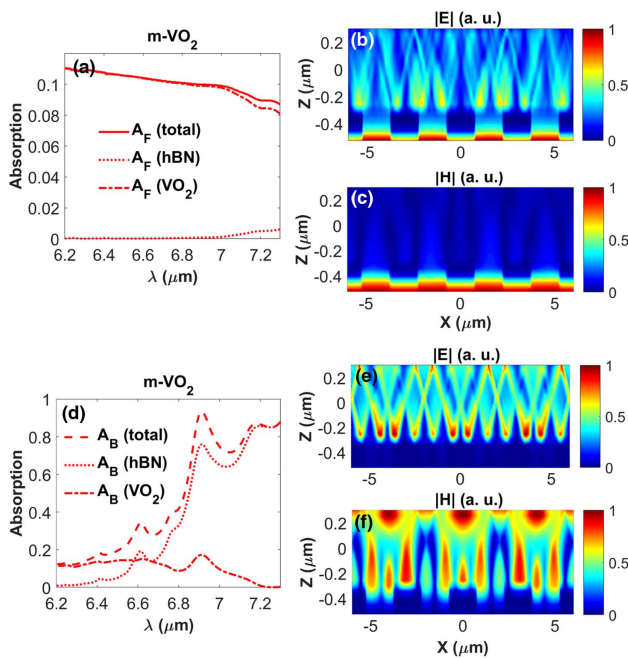
aforementioned conditions for achieving AT with $T_F > T_B$. On the other hand, for the m-VO_2 case, a negligible portion of light can transmit through the structure due to an increase of reflection (from the VO_2/Au hybrid grating) for the forward illumination and an increase of absorption for the backward one. The asymmetric transmission factor (ATF) of the device, which can be defined as $|T_F - T_B| \times 100\%$, is illustrated in Fig. 3(c) for both the i-VO_2 and m-VO_2 cases by the solid blue and solid red lines, respectively. It is seen that the ATF of the device can reach 40% for the dielectric phase of VO_2 and it is switched to almost zero values once the structure is heated up to 85°C at the m-VO_2 phase. Near-field mode profiles of light passing through the i-VO_2 metamaterial for forward and backward illuminations at $\lambda = 6.6$ µm are also presented in Figs. 3(d) and 3(e), respectively. It is seen from the mode profiles that supporting HP^2-IMT polariton rays inside hBN, which resemble those HP^2 modes of a bare film of hBN [32,33], is responsible for the general response of the device.

In agreement with Figs. 3(a) and 3(b), in Figs. 3(f) and 3(g) we investigate the absorption features of the structure depicted in Fig. 1(d) (without graphene) for the opposite directions of illumination and the insulator and metal phases of VO_2. Figure 3(f) shows that for the i-VO_2 case, backward absorption (A_B) is stronger than the forward one (A_F) for $\lambda > 6.8$ µm. Further investigations into the results prove that the excitation

of hyperbolic modes inside hBN are mostly responsible for the absorption of the structure for backward illumination, while for forward illumination, lossy modes of the insulating VO_2 take the lead for absorption for $\lambda < 6.8$ µm. For the m-VO_2 case, the absorptive feature of the device is more interesting. In this case, as shown in Fig. 3(g), for forward illumination the structure is mostly non-absorptive and negligibly transmittive [see Fig. 3(b)], since the hybrid VO_2/Au grating acts as a reflector layer. On the other hand, for backward illumination, due to the strong confinement of the high-β low-propagating hybrid HP^2-IMT modes inside the hBN layer, the device presents a nearly perfect absorption resonance at 6.8 µm. Consequently, by comparing the dashed blue and dashed red lines shown in Figs. 3(f) and 3(g), it is understood that there is a 50% increase in the backward resonant absorption of the device once the phase of VO_2 is switched from insulator to metal, and thus nearly perfect absorption is obtained. Therefore, representing the AT attribute for the i-VO_2 case and the nearly perfect resonant absorption feature for the m-VO_2 case gives the device a bi-functional characteristic beneficial for some practical purposes. To obtain more insight into the nature of the nearly perfect resonant absorption feature of the device for the m-VO_2 backward illumination, we investigate how the hBN and VO_2 layers contribute to total absorption of the metamaterial (see Fig. 4).

Figure 4(a) illustrates total absorption (solid red line) and contributions of the hBN layer (dashed–dotted red line) and the hybrid VO_2/Au grating layer (dotted red line) to the total absorption of the metamaterial for forward illumination. In agreement with the above-mentioned points, since the hybrid VO_2/Au grating layer is mostly reflective for the metallic phase of VO_2, total absorption is less than 10% for forward illumination. Therefore, light is generally absorbed inside the hybrid VO_2/Au grating for this case. In support of this statement, it is observed from the mode profiles shown in Figs. 4(b) and 4(c) that $|E|$ and $|H|$ are almost concentrated in the VO_2 layers. Note that in the mode profiles shown in Fig. 4, hBN and hybrid VO_2/Au grating layers are placed in the $-0.3 < z$ (µm) < 0.3 and $-0.5 < z$ (µm) < -0.3 regions. In contrast to the forward illumination, it is seen in Fig. 4(d) that for the m-VO_2 backward illumination, absorption in hBN (dotted red line) is the most contributed portion in total absorption value (dashed red line), while the share of the VO_2/Au hybrid grating (dashed–dotted red line) is less noticeable. For simplicity, the absorption portion of the VO_2/Au hybrid grating is labeled as VO_2 in Figs. 4(a) and 4(b). $|E|$ and $|H|$ mode profiles—shown at $\lambda = 6.9$ µm (wavelength of the nearly perfect resonant absorption)—support the latter claim [see Figs. 4(b) and 4(c)] and verify this point that support of the hybrid HP^2-IMT polariton rays in the hBN layer takes the lead for the observation of the nearly perfect absorption feature, as shown in panels Figs. 4(e) and 4(f).

As we schematically illustrated in Fig. 1(d), the HGH heterostructure is the building block component of our final metamaterial design. The design is composed of an unpatterned HGH heterostructure that is bounded by the Ge grating on the upper side and the hybrid VO_2/Au grating on the lower side and is placed on top of an Al_2O_3 substrate. In addition to having the bi-functional feature, another advantageous characteristic of this design is its bi-tunable attribute. This attribute is provided by the gate tunable capability of graphene and the thermally switchable/tunable feature of VO_2. It is noteworthy that graphene can also be tuned by external thermal stimuli; however, our calculations prove that this effect is not as effective as the gating feature for tuning the optical response of the metamaterial device under our consideration here. To be more specific, by taking $T = 300$ K and 358 K in the optical conductivity of graphene, we have examined analytical and numerical results shown in Fig. 5 and observed negligible differences.

After obtaining sufficient insight into the effect of the metal–insulator switching feature of VO_2 on the transmission and absorption attributes of the device, we are now at the stage to investigate the effect of the presence of graphene in the calculations. It has been theoretically/experimentally proved that in graphene/hBN heterostructures, monolayer graphene can efficiently impact the dispersion characteristics of the HP^2 modes of an hBN film with thickness of up to 300 nm [35]. In this case, hybrid HP^3 and SP^3 modes can be supported, respectively, inside and outside of the hBN RS bands. Therefore, to obtain the most effective efficiency of the device—i.e., to achieve HP^2-SP^2 coupling together with a fair absorption of the hBN film—we consider the thickness of each hBN layer in the HGH structure as 300 nm, so the total thickness of the structure is $t_h \cong 600$ nm [check t_h in Fig. 1(c)]. Taking $\mu = 0.5$ eV (otherwise stated) and considering a multilayer graphene ($N_g = 10$) in the following calculations, the dispersion characteristics of the HP^3-IMT modes supported by the HGH/VO_2 heterostructure for the i-VO_2 and m-VO_2 cases are illustrated in Figs. 5(a) and 5(b). Note that dispersion of the modes of the bare hBN (solid black lines), i-VO_2 HV (solid blue lines), and m-VO_2 HV (solid red lines) structures are reshown in Figs. 5(a) and 5(b) for ease of comparison. Moreover, the dispersion of the hybrid HP^3-IMT modes [obtained by Eq. (4)] is illustrated as solid pink lines for both the i-VO_2 and m-VO_2 cases in Figs. 5(a) and 5(b). As it is observed from these panels, the presence of multilayer graphene has a noticeable effect on the modes' dispersion. This gives us the opportunity for effective tuning of the hybrid modes supported by the HGH heterostructure via the gating feature of graphene.

When considering graphene in the numerical calculations, it is understood that the presence of graphene keeps the strength of the resonant transmission response of the metamaterial [shown in Fig. 1(d)] for forward illumination, as we compare the solid blue line in Fig. 5(c) to the one presented in Fig. 3(a), while keeping T_B very low. This leads to achieving almost 40% of the ATF at $\lambda = 6.45$ µm, as shown in Fig. 5(d). Moreover, by comparing the solid blue line (with graphene) and solid black line (without graphene) in this figure, it is understood that the presence of graphene can considerably tune the ATF of the designed metamaterial through modifying μ. Figure 5(e) illustrates the ATF of the device as a function of
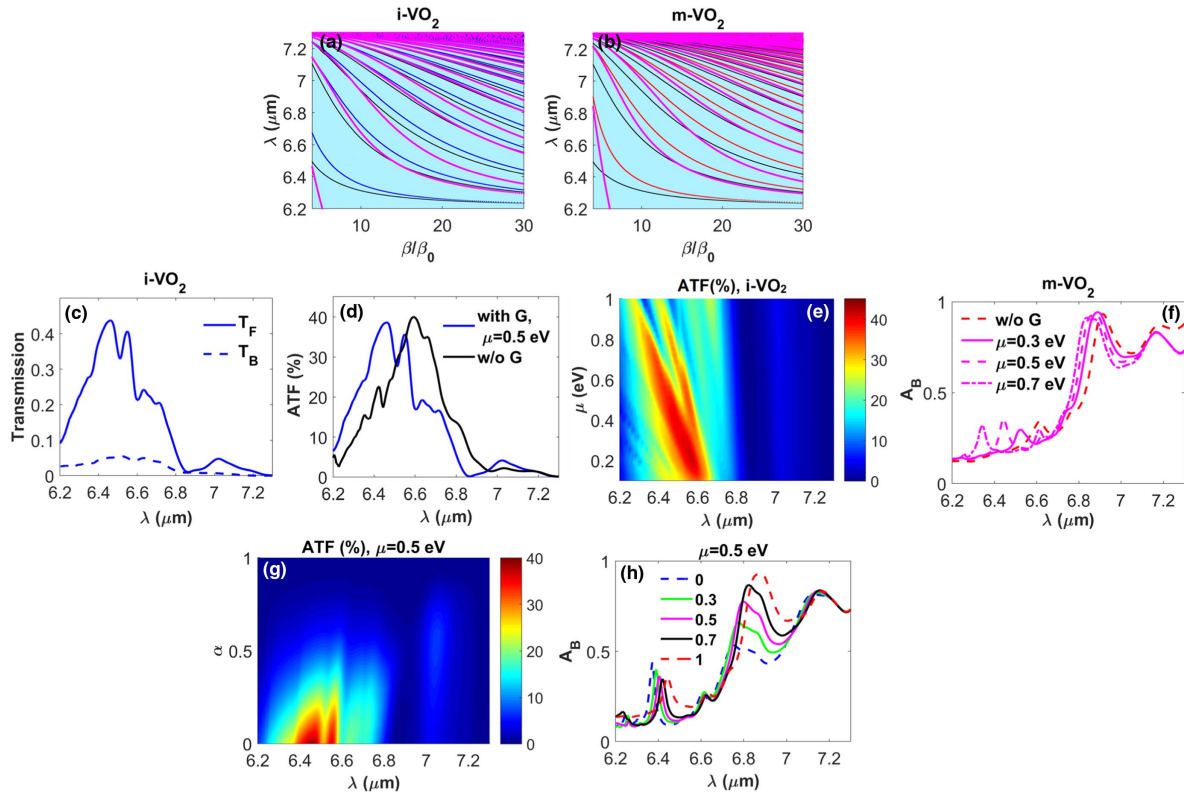
Fig. 4. In agreement with Fig. 3(g), (a) and (d) present total absorption [solid line in (a) and dashed line in (d)], the hBN contribution in total absorption (dotted lines), and absorption in the hybrid VO_2/Au grating (dashed–dotted line) for forward and backward illumination, respectively. (b), (c) $|E|$ and (e), (f) $|H|$ profiles of the hybrid HP^2-IMT modes at $\lambda = 6.9$ µm.

Fig. 5. Bi-tunable characteristics of the metamaterial. (a) and (b) are the same as Figs. 2(a) and 2(b) while the dispersion of the HP^3-IMT modes (solid pink lines) supported by the structure shown in Fig. 1(c) are also illustrated for $N_g = 10$, $\mu = 0.5$ eV, and $\tau = 1$ ps. (c) Forward (solid blue line) and backward (dashed blue line) transmission of the device for the i-VO$_2$ case. (d) ATF of the metamaterial with (solid blue line) and without (solid black line) the presence of multilayer graphene. (e) ATF as a function of the chemical potential of graphene and wavelength for the i-VO$_2$ case. (f) Tunable feature of backward absorption of the device for the m-VO$_2$ case, without graphene (dashed red line), and with the presence of graphene for $\mu = 0.3$ eV (solid pink line), $\mu = 0.5$ eV (dashed pink line), and $\mu = 0.7$ eV (dashed–dotted pink line). (g) ATF of the i-VO$_2$ metamaterial as a function of metallic fraction coefficient (α) and wavelength. (h) Backward absorption of the m-VO$_2$ metamaterial is depicted for different values of α.

the wavelength and chemical potential of graphene for the i-VO$_2$ case. It is observed that, (i) in agreement with Fig. 5(d), increasing the chemical potential of the graphene layers leads to the blueshifting of the maximum value of the ATF inside the RS-II band of hBN, and (ii) the ATF of the device can reach 45% for $\mu \sim 0.2$ eV. As discussed above, supporting nearly perfect resonant absorption for the m-VO$_2$ case is another eye-catching feature of our design. Figure 5(f) proves that the resonant absorption response can be dynamically tuned, within the wavelength region around 6.8 μm, via modifying the chemical potential of graphene.

Instead of the switching effect for the insulator and metal phases of VO$_2$, it is also possible to take into account for the dynamic phase evolutions of the IMT of VO$_2$ by considering the intermediate states in the calculations. If we consider the insulating and metal phases of VO$_2$ as i-VO$_2$ (room temperature, $\alpha = 0$ and ε_{ins}) and m-VO$_2$ ($T = 358$ K, $\alpha = 1$ and ε_{met}), the permittivity of the intermediate states (ε_{inter}) can be described by employing a Lorentz–Lorenz effective medium model as [41]

$$\frac{\varepsilon_{inter} - 1}{\varepsilon_{inter} + 2} = \alpha \frac{\varepsilon_{met} - 1}{\varepsilon_{met} + 2} + (1 - \alpha) \frac{\varepsilon_{insul} - 1}{\varepsilon_{insul} + 2}, \quad (7)$$

where α is the metallic fraction coefficient. Consequently, by taking different values of α in the calculations, it is possible to dynamically investigate the effect of IMT evolution on the transmission and absorption features of the designed metamaterial, see Figs. 5(e) and 5(h).

4. CONCLUSION

We have analytically examined the hybridization of high-β hyperbolic phonon polaritons of hBN with IMT of VO$_2$ in a bare hBN/VO$_2$ heterostructure for both i-VO$_2$ and m-VO$_2$ phases and TM polarization; i.e., the support of HP^2-IMT modes. Based on the understanding of hybridized high-β modes of the system, we have numerically designed a bi-functional metamaterial composed of film of hBN bounded by Ge and hybrid VO$_2$/Au gratings for operation in the MIR range. The bi-functional metamaterial enables broadband and efficient AT with ATF exceeding 40% for the i-VO$_2$ case, while for the m-VO$_2$ case it exhibits nearly perfect resonant absorption for backward illumination (and also almost zero transmission for both directions of illumination). In other words, the i-VO$_2$ case has practical use for AT, while the m-VO$_2$ case can be employed to achieve nearly perfect resonant absorption.

Consequently, the thermal counterpart of our design is mainly responsible for the switch between AT and nearly perfect absorption functionalities. It is noteworthy that obtaining AT by employing the high-β modes of hBN as a natural hyperbolic material can also be a practical advantage over achieving AT using those modes supported by HMMs [20]. Moreover, we have analytically examined HP^3-IMT modes in a bare hBN/graphene/hBN/VO$_2$ heterostructure. Then, by embedding multilayer graphene into the above-mentioned grating-bounded design—i.e., the HGH heterostructure bounded by the Ge and VO$_2$/Au gratings—and considering the intermediate states of VO$_2$ in the calculations during IMT, bi-tunable AT (ATF exceeding 45%) and resonant absorption characteristics via changes in μ of graphene have been achieved. The findings presented in this paper can be realized in practice, being beneficial for MIR sensing (e.g., see Refs. [50,51]), optical isolation [3], and thermal emission (see, e.g., Ref. [25] and the references therein) applications.

REFERENCES

1. V. A. Fedotov, P. L. Mladyonov, S. L. Prosvirnin, A. V. Rogacheva, Y. Chen, and N. I. Zheludev, "Asymmetric propagation of electromagnetic waves through a planar chiral structure," Phys. Rev. Lett. 97, 167401 (2006).
2. A. E. Serebryannikov, "One-way diffraction effects in photonic crystal gratings made of isotropic materials," Phys. Rev. B 80, 155117 (2009).
3. L. Bi, J. Hu, P. Jiang, D. H. Kim, G. F. Dionne, L. C. Kimerling, and C. A. Ross, "On-chip optical isolation in monolithically integrated nonreciprocal optical resonators," Nat. Photonics 5, 758–762 (2011).
4. M. Scalora, J. P. Dowling, C. M. Bowden, and M. J. Bloemer, "The photonic band edge optical diode," J. Appl. Phys. 76, 2023–2026 (1994).
5. M. Stolarek, D. Yavorskiy, R. Kotyński, C. J. Z. Rodríguez, J. Lusakowski, and T. Szoplik, "Asymmetric transmission of terahertz radiation through a double grating," Opt. Lett. 38, 839–841 (2013).
6. S. Cakmakyapan, A. E. Serebryannikov, H. Caglayan, and E. Ozbay, "Spoof-plasmon relevant one-way collimation and multiplexing at beaming from a slit in metallic grating," Opt. Express 20, 26636–26648 (2012).
7. L. Fan, J. Wang, L. T. Varghese, H. Shen, B. Niu, Y. Xuan, A. M. Weiner, and M. Qi, "An all-silicon passive optical diode," Science 335, 447–450 (2012).
8. V. Liu, D. A. B. Miller, and S. Fan, "Ultra-compact photonic crystal waveguide spatial mode converter and its connection to the optical diode effect," Opt. Express 20, 28388–28397 (2012).
9. A. E. Serebryannikov, M. Beruete, M. Mutlu, and E. Ozbay, "Multiband one-way polarization conversion in complementary split-ring resonator based structures by combining chirality and tunneling," Opt. Express 23, 13517–13529 (2015).
10. W. Fan, Y. Wang, R. Zheng, D. Liu, and J. Shi, "Broadband high efficiency asymmetric transmission of achiral metamaterials," Opt. Express 23, 19535–19541 (2015).
11. B. Tang, Z. Li, Z. Liu, F. Callewaert, and K. Aydin, "Broadband asymmetric light transmission through tapered metallic gratings at visible frequencies," Sci. Rep. 6, 39166 (2016).
12. A. Ozer, H. Kocer, and H. Kurt, "Broadband and polarization-independent asymmetric transmission of visible light through a three-dimensional trapezoidal metallic metasurface," J. Opt. Soc. Am. B 35, 2111–2117 (2018).
13. X. Li, W. Liu, and W. She, "Asymmetric optical transmission through silver film with a hyperbolic air hole," J. Opt. Soc. Am. B 35, 886–891 (2018).
14. Y. Zhou, Y. Dong, R. Fan, Q. Hu, R. Peng, and M. Wang, "Asymmetric transmission of terahertz waves through a graphene-loaded metal grating," J. Appl. Phys. 105, 041114 (2014).
15. Z. Li, W. Liu, H. Cheng, S. Chen, and J. Tian, "Tunable dual-band asymmetric transmission for circularly polarized waves with graphene planar chiral metasurfaces," Opt. Lett. 41, 3142–3145 (2016).
16. H. Jiang, W. Zhao, and Y. Jiang, "High-efficiency tunable circular asymmetric transmission using dielectric metasurface integrated with graphene sheet," Opt. Express 25, 19732–19739 (2017).
17. A. Serebryannikov, H. Hajian, M. Beruete, E. Ozbay, and G. Vandenbosch, "Tunable deflection and asymmetric transmission of THz waves using a thin slab of graphene-dielectric metamaterial, with and without ENZ components," Opt. Mater. Express 8, 3887–3898 (2018).
18. A. E. Serebryannikov and E. Ozbay, "One-way Rayleigh-Wood anomalies and tunable narrowband transmission in photonic crystal gratings with broken structural symmetry," Phys. Rev. B 87, 053804 (2013).
19. L. Zinkiewicz, J. Haberko, and P. Wasylczyk, "Highly asymmetric near infrared light transmission in an all-dielectric grating-on-mirror photonic structure," Opt. Express 23, 4206–4211 (2015).
20. T. Xu and H. J. Lezec, "Visible-frequency asymmetric transmission devices incorporating a hyperbolic metamaterial," Nat. Commun. 5, 4141 (2014).
21. C. M. Watts, X. Liu, and W. J. Padilla, "Metamaterial electromagnetic wave absorbers," Adv. Mater. 24, OP98–OP120 (2012).
22. H. Deng, Z. Li, L. Stan, D. Rosenmann, D. Czaplewski, J. Gao, and X. Yang, "Broadband perfect absorber based on one ultrathin layer of refractory metal," Opt. Lett. 40, 2592–2595 (2015).
23. A. Ghobadi, H. Hajian, B. Butun, and E. Ozbay, "Strong light-matter interaction in lithography-free planar metamaterial perfect absorbers," ACS Photon. 5, 4203–4221 (2018).
24. B. Zhao and Z. M. Zhang, "Resonance perfect absorption by exciting hyperbolic phonon polaritons in 1D hBN gratings," Opt. Express 25, 7791–7796 (2017).
25. H. Hajian, A. Ghobadi, B. Butun, and E. Ozbay, "Nearly perfect resonant absorption and coherent thermal emission by hBN-based photonic crystals," Opt. Express 25, 31970–31987 (2017).
26. R. Alaee, M. Farhat, C. Rockstuhl, and F. Lederer, "A perfect absorber made of a graphene micro-ribbon metamaterial," Opt. Express 20, 28017–28024 (2012).
27. H. Li, C. Ji, Y. Ren, J. Hu, M. Qin, and L. Wang, "Investigation of multiband plasmonic metamaterial perfect absorbers based on graphene ribbons by the phase-coupled method," Carbon 141, 481–487 (2019).
28. H. Li, M. Qin, L. Wang, X. Zhai, R. Ren, and J. Hu, "Total absorption of light in monolayer transition-metal dichalcogenides by critical coupling," Opt. Express 25, 31612–31621 (2017).
29. H. Li, Y. Ren, J. Hu, M. Qin, and L. Wang, "Wavelength-selective wide-angle light absorption enhancement in monolayers of transition-metal dichalcogenides," J. Lightwave Technol. 36, 3236–3241 (2018).
30. P. Huo, Y. Liang, S. Zhang, and T. Xu, "Hybrid metasurface for broadband enhancing optical absorption and Raman spectroscopy of graphene," Opt. Mater. Express 7, 3591–3597 (2017).
31. Z. Zhang, Z. Yu, Y. Liang, and T. Xu, "Dual-band nearly perfect absorber at visible frequencies," Opt. Mater. Express 8, 463–468 (2018).
32. J. D. Caldwell, A. V. Kretinin, Y. Chen, V. Giannini, M. M. Fogler, Y. Francescato, C. T. Ellis, J. G. Tischler, C. R. Woods, A. J. Giles, M. Hong, K. Watanabe, T. Taniguchi, S. A. Maier, and K. S. Novoselov,

"Subdiffractional volume-confined polaritons in the natural hyperbolic material hexagonal boron nitride," Nat. Commun. **5**, 5221 (2014).

33. S. Dai, Z. Fei, Q. Ma, A. S. Rodin, M. Wagner, A. S. McLeod, M. K. Liu, W. Gannett, W. Regan, K. Watanabe, T. Taniguchi, M. Thiemens, G. Dominguez, A. H. Castro Neto, A. Zettl, F. Keilmann, P. Jarillo-Herrero, M. M. Fogler, and D. N. Basov, "Tunable phonon polaritons in atomically thin van der Waals crystals of boron nitride," Science **343**, 1125–1129 (2014).

34. F. J. Alfaro-Mozaz, P. Alonso-González, S. Vélez, I. Dolado, M. Autore, S. Mastel, F. Casanova, L. E. Hueso, P. Li, A. Y. Nikitin, and R. Hillenbrand, "Nanoimaging of resonating hyperbolic polaritons in linear boron nitride antennas," Nat. Commun. **8**, 15624 (2017).

35. S. Dai, Q. Ma, M. K. Liu, T. Andersen, Z. Fei, M. D. Goldflam, M. Wagner, K. Watanabe, T. Taniguchi, M. Thiemens, F. Keilmann, G. C. A. M. Janssen, S.-E. Zhu, P. Jarillo-Herrero, M. M. Fogler, and D. N. Basov, "Graphene on hexagonal boron nitride as a tunable hyperbolic metamaterial," Nat. Nanotechnol. **10**, 682–686 (2015).

36. A. Kumar, T. Low, K. H. Fung, P. Avouris, and N. X. Fang, "Tunable light-matter interaction and the role of hyperbolicity in graphene-hBN system," Nano Lett. **15**, 3172–3180 (2015).

37. H. Hajian, A. Ghobadi, S. Abedini Dereshgi, B. Butun, and E. Ozbay, "Hybrid plasmon-phonon polariton bands in graphene-hexagonal boron nitride metamaterials," J. Opt. Soc. Am. B **34**, D29–D35 (2017).

38. H. Hajian, A. Ghobadi, B. Butun, and E. Ozbay, "Tunable, omnidirectional, and nearly perfect resonant absorptions by a graphene-hBN-based hole array metamaterial," Opt. Express **26**, 16940–16954 (2018).

39. M. J. Dicken, K. Aydin, I. M. Pryce, L. A. Sweatlock, E. M. Boyd, S. Walavalkar, J. Ma, and H. A. Atwater, "Frequency tunable near-infrared metamaterials based on VO₂ phase transition," Opt. Express **17**, 18330–18339 (2009).

40. H. Kocer, S. Butun, E. Palacios, Z. Liu, S. Tongay, D. Fu, K. Wang, J. Wu, and K. Aydin, "Intensity tunable infrared broadband absorbers based on VO₂ phase transition using planar layered thin films," Sci. Rep. **5**, 13384 (2015).

41. Z. Liu, B. Banar, S. Butun, H. Kocer, K. Wang, J. Scheuer, J. Wu, and K. Aydin, "Dynamic infrared thin-film absorbers with tunable absorption level based on VO₂ phase transition," Opt. Mater. Express **8**, 2151–2158 (2018).

42. H. Liu, J. Lu, and X. R. Wang, "Metamaterials based on the phase transition of VO₂," Nanotechnology **29**, 024002 (2018).

43. C. Wan, E. H. Horak, J. King, J. Salman, Z. Zhang, Y. Zhou, P. Roney, B. Gundlach, S. Ramanathan, R. H. Goldsmith, and M. A. Kats, "Limiting optical diodes enabled by the phase transition of vanadium dioxide," ACS Photon. **5**, 2688–2692 (2018).

44. N. Antonellis, R. Thomas, M. A. Kats, I. Vitebskiy, and T. Kottos, "Asymmetric transmission in photonic structures with phase change components," arXiv:1806.07514v1 (2018).

45. S. Dai, J. Zhang, Q. Ma, S. Kittiwatanakul, A. S. McLeod, X. Chen, S. N. Gilbert Corder, K. Watanabe, T. Taniguchi, J. Lu, Q. Dai, P. Jarillo-Herrero, M. K. Liu, and D. N. Basov, "Phase-change hyperbolic heterostructures for nanopolaritonics: a case study of hBN/VO₂," Adv. Mater. (to be published). Available: https://doi.org/10.1002/adma.201900251.

46. T. G. Folland, A. Fali, S. T. White, J. R. Matson, S. Liu, N. A. Aghamiri, J. H. Edgar, R. F. Haglund, Y. Abate, and J. D. Caldwell, "Reconfigurable mid-infrared hyperbolic metasurfaces using phase-change materials," arXiv:1805.08292v1 (2018).

47. Lumerical Solutions., http://www.lumerical.com/tcadproducts/fdtd.

48. L. A. Falkovsky, "Optical properties of graphene," J. Phys. Conf. Ser. **129**, 012004 (2008).

49. E. D. Palik, *Handbook of Optical Constants of Solids* (Elsevier, 1988).

50. A. Lochbaum, Y. Fedoryshyn, A. Dorodnyy, U. Koch, C. Hafner, and J. Leuthold, "On-chip narrowband thermal emitter for mid-IR optical gas sensing," ACS Photon. **4**, 1371–1380 (2017).

51. J. A. Mason, G. Allen, V. A. Podolskiy, and D. Wasserman, "Dual-band perfect absorber for multispectral plasmon-enhanced infrared spectroscopy," ACS Nano **6**, 7998–8006 (2012).